Dénes Takács[1]

Research Group on Dynamics of Vehicles and
Machines,
Hungarian Academy of Sciences,
Budapest H-1521, Hungary
e-mail: takacs@mm.bme.hu

Gábor Stépán

Department of Applied Mechanics,
Budapest University of Technology and
Economics,
Budapest H-1521, Hungary
e-mail: stepan@mm.bme.hu

Experiments on Quasiperiodic Wheel Shimmy

The lateral vibration of towed wheels—so-called shimmy—is one of the most exciting phenomena of vehicle dynamics. We give a brief description of a simple rig of elastic tire that was constructed for laboratory measurements. A full report is given on the experimental investigation of this rig from the identification of system parameters to the validation of stability boundaries and vibration frequencies of shimmy motion. The experimental results confirm the validity of those tire models that include delay effects. A peculiar quasiperiodic oscillation detected during the experiments is explained by numerical simulations of the nonlinear time-delayed mathematical model.
[DOI: 10.1115/1.3124786]

1 Introduction

The lateral vibration of towed wheels (called shimmy) is a well-known phenomenon in vehicle dynamics. The ultimate elimination of shimmy is a problem for engineers during the design of airplane nose gears, motorcycles, trailers, etc. A recent overview about the landing gear dynamics can be found in Ref. [1] with particular reference to shimmy. In spite of the fact that the problem has been known and studied for almost a century [2,3], the elimination of shimmy is one of the most critical part of the landing gear design [4–6]. Shimmy is also well-known as one of the most dangerous vibration problem (also called as "wobble") of motorcycles [7,8]. Accidents involving trailers and caravans are often originated in the so-called "waving" of the vehicles [9,10].

Shimmy can be related to the elasticity of the tire [11–14] or to the elasticity of the suspension system [15,16]. Some basic properties of shimmy, such as the existence of an unstable limit cycle in certain speed ranges, can be demonstrated by using rigid wheel and elastic caster models [17].

Nevertheless, the majority of vehicles is rolling on pneumatic tires and the elasticity of the tire is usually much larger than the lateral elasticity of the suspension system. A widely used model that takes into account the elasticity of the wheel applies the well-studied creep-force idea [18,19] often mentioned as Pacejka's magic formula, in practice. Basically, this creep-force idea means the insertion of a stationary submodel into the dynamical model of shimmy, which gives satisfactory results in a wide range of parameters. Still, even some qualitative phenomena can hardly be explained this way, including the quasiperiodicity of shimmy at low towing speeds.

In this study, a simple elastic tire model with one rigid-body degree-of-freedom is investigated by means of a different mechanical model. Some of the theoretical analysis and aspects of this model are published in [14]. To validate the surprising analytical results, experiments are carried out: at the intersection of the stability boundaries in the parameter space of shimmy, quasiperiodic self-excited vibrations are observed with time varying frequency content.

Our analysis can successfully explain some of the frequency components, but the spectra of the recorded vibration signals contain some theoretically unexplained frequencies, too. This is caused by the nonlinear effect of partial sliding within the tire/ground contact region. Since this nonlinearity is not amenable to analytical studies, numerical simulations are carried out with special attention for the partial sliding effect. The simulated and measured spectra are compared and harmonized leading to a clear explanation of the experimental results showing quasiperiodic shimmy at low towing speeds.

2 Mechanical Model

The mechanical model in question is taken from Ref. [14]. The elastic tire is towed by a rigid caster of length l on the steady ground by constant velocity v, as it is shown in Fig. 1. The contact patch between the ground and the tire is modeled by a contact line of length $2a$. In this way the lateral deformation of the tire is described by the displacement function $q(x,t)$ of this contact line relative to the plane of the wheel. The coordinate x describes the position of the contact points in the contact line, where the coordinate system (x,y,z) is attached to the caster, and t stands for the time.

The equation of motion is given by the integrodifferential equation (IDE) as follows:

$$J_A \ddot{\psi}(t) = -k \int_{-a}^{a} (l-x)q(x,t)\mathrm{d}x - b \int_{-a}^{a} (l-x)\frac{\mathrm{d}}{\mathrm{d}t}q(x,t)\mathrm{d}x \quad (1)$$

where dot refers to derivation with respect to time. The mass moment of inertia is J_A (kg m^2) with respect to the z axis at the articulation point, k (N/m^2) is the specific lateral stiffness of the tire, and b (Ns/m^2) is the specific lateral damping factor of the tire along the contact line.

We briefly summarize the derivation of the kinematical constraint leading to a delay effect based on Ref. [14]. In case of rolling, the tire elements stick to the ground and have steady position relative to the ground during contact. The position of a tire point P contacted to the ground can be given in the ground-fixed coordinate system (X,Y,Z):

$$\begin{bmatrix} X(x,t) \\ Y(x,t) \end{bmatrix} = \begin{bmatrix} vt - (l-x)\cos\psi(t) - q(x,t)\sin\psi(t) \\ -(l-x)\sin\psi(t) + q(x,t)\cos\psi(t) \end{bmatrix} \quad (2)$$

for $x \in [-a,a]$. The total differentiation of this position vector with respect to time gives the velocities of the contact points taken to be zero to enforce the no-slip condition,

$$\frac{\mathrm{d}}{\mathrm{d}t}\begin{bmatrix} X(x,t) \\ Y(x,t) \end{bmatrix} = \begin{bmatrix} 0 \\ 0 \end{bmatrix} \quad (3)$$

for $x \in [-a,a]$. The manipulation of these two scalar equations leads to the kinematical constraint of rolling given by a partial differential equation (PDE)
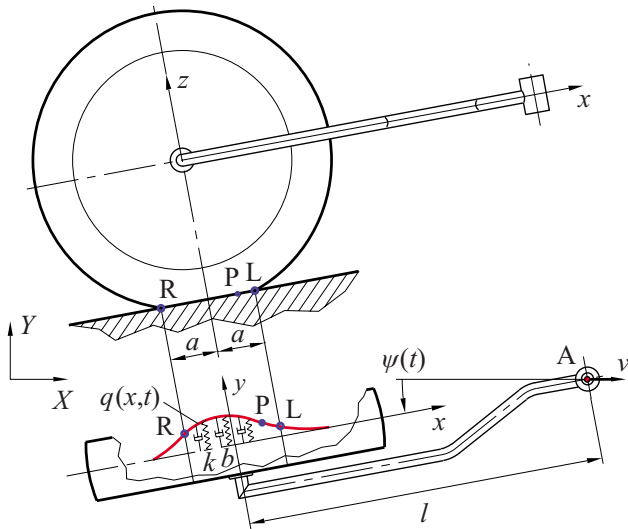
Fig. 1 Mechanical model of towed tire

$$\dot{q}(x,t) = v \sin \psi(t) + (l-x)\dot{\psi}(t) + q'(x,t)(v \cos \psi(t) - q(x,t)\dot{\psi}(t)) \tag{4}$$

with $x \in [-a, a]$ and $t \in [t_0, \infty)$ for the lateral direction. Prime refers to derivation with respect to space variable x. In case of the simplest brush model of the tire (see Ref. [18]), the corresponding boundary condition is given by $q(a,t)=0$ due to the zero deformation at the leading edge.

The equation of motion (Eq. (1)) and the kinematical constraint (Eq. (4)) describe the system as a coupled IDE-PDE system. Since the contact points are sticking to the ground in (X, Y, Z), they travel backwards relative to the caster in (x, y, z). This gives the physical explanation for the introduction of the traveling wave solution

$$\begin{bmatrix} X(x,t) \\ Y(x,t) \end{bmatrix} = \begin{bmatrix} X(a, t - \tau(x)) \\ Y(a, t - \tau(x)) \end{bmatrix} \tag{5}$$

where the time $\tau(x)$ is needed for a tire point at the leading edge L at $x=a$ to travel backward relative to the caster to the actual position P at x_P. Accordingly, the recent history of the wheel motion is stored in the deformation of the contact area. Figure 2 represents this memory effect of the tire: the lateral forces depend
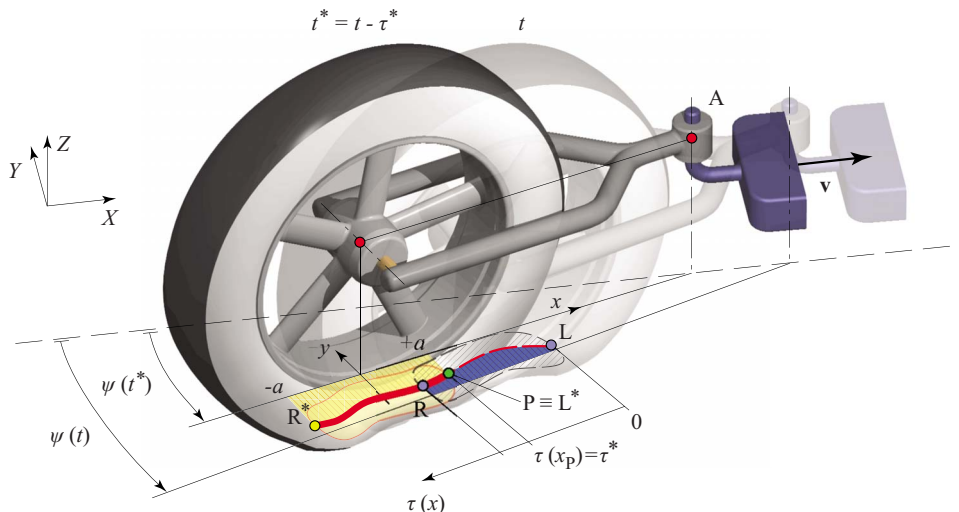
on the tire contact point positions determined by the wheel leading edge positions in the past, when these points were put down to the ground.

The traveling wave solution and the time delay can be determined in closed form if we consider small oscillations only. By using the linearized form of Eq. (2) in Eq. (5), we obtain the time delay in the physically obvious form

$$\tau(x) \approx \frac{a-x}{v} \tag{6}$$

The traveling wave solution of small motions can be calculated with the help of the following boundary condition $q(a,t)=0$:

$$q(x,t) = (l-x)\psi(t) - (l-a)\psi(t - \tau(x)) \tag{7}$$

which satisfies the linearized form of the kinematical constraint (Eq. (4)), of course.

When the traveling wave solution (Eq. (7)) is substituted into the IDE (Eq. (1)), the linearized IDE-PDE system can be transformed into the linear delay-differential equation (DDE)

$$J_A \ddot{\psi}(t) + 2ab\left(l^2 + \frac{a^2}{3}\right)\dot{\psi}(t) + 2a\left(k\left(l^2 + \frac{a^2}{3}\right) + bvl\right)\psi(t)$$
$$= (l-a)vk \int_0^{\frac{2a}{v}} (l-a+v\tau)\psi(t-\tau)d\tau \tag{8}$$

The nonlinear form of this DDE can be found in Ref. [14] without damping.

Introduce the dimensionless towing length and the dimensionless towing speed as follows:

$$L = l/a \quad \text{and} \quad V = v/(4\pi a f_n) \tag{9}$$

respectively, where f_n is the natural frequency of the undamped system at zero towing speed. The corresponding damping ratio of the system is

$$\zeta = f_n b\pi/k \tag{10}$$

With the new parameters and with the dimensionless time $T = v/(2a)t$ and $\vartheta = -v/(2a)\tau$, the dimensionless equation of this delayed oscillator assumes the form

$$V^2\ddot{\psi}(T) + 2\zeta V\dot{\psi}(T) + \left(1 + \frac{4\zeta VL}{L^2 + 1/3}\right)\psi(T)$$
$$= \frac{L-1}{L^2 + 1/3}\int_{-1}^{0} (L-1-2\vartheta)\psi(T+\vartheta)d\vartheta \tag{11}$$

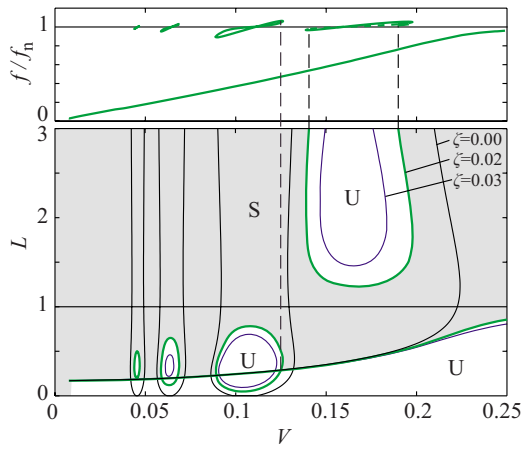**Fig. 2 Rolling of the elastic tire**

Fig. 3 Linear stability chart and self-excited vibration frequencies

3 Linear Stability

Stationary rolling is given by the trivial solution $\psi(T) \equiv 0$. The substitution of the trial solution $\psi(T) = \psi_0 e^{\lambda T}$ into Eq. (11)—or the Laplace transformation—leads to the characteristic function

$$D(\lambda) = V^2 \lambda^2 + 2\zeta V \lambda + 1 + \frac{4\zeta V L}{L^2 + 1/3}$$
$$- \frac{L-1}{L^2 + 1/3}\left(L\frac{1-e^{-\lambda}}{\lambda} - \frac{1+e^{-\lambda}}{\lambda} + 2\frac{1-e^{-\lambda}}{\lambda^2} \right) \quad (12)$$

The linear stability boundaries can be determined with the D-subdivision method [20]. The substitution of the pure imaginary $\lambda = i\omega$ into Eq. (12) may refer to Hopf bifurcation. $D(i\omega)$ is separated to real and imaginary parts. For a fixed angular frequency ω and damping ratio ζ, the values of V and L can be calculated numerically with the help of the equations Re $D(i\omega) = 0$ and Im $D(i\omega) = 0$, where ω represents the angular frequency of the self-excited vibration arising at the stability limit. This method leads to the determination of the stability boundaries in the (V, L) plane parametrized by ω for a chosen damping ratio ζ. To decide the sense of the stability of the separated regions, the stability criterion in Ref. [20] can be used.

The stability chart of the system is given in Fig. 3, where the stable areas are shaded for the damping ratio $\zeta = 0.02$. The self-excited vibration frequencies f at the stability boundaries are also plotted relative to the natural frequency. At the intersections of two stability boundaries a so-called double Hopf bifurcation points exist. At these parameter points, two pairs of pure imaginary complex conjugate characteristic exponents exist with imaginary parts referring to two different vibration frequencies. The corresponding self-excited vibrations are quasiperiodic. Our goal is to observe these quasiperiodic oscillations experimentally on a rig that has only one rigid-body degree-of-freedom. The experiments should emphasize the essential role of delay effect in tire dynamics.

4 Experiments

The experimental study of the self-excited vibrations started with a thorough parameter identification of the rig constructed specially for these shimmy experiments.

4.1 Tire Parameter Identification. First, the stiffness and damping parameters of the selected tire were measured. After fixing a certain pneumatic tire pressure, the wheel was placed in a rigid frame and the contact length was adjusted with the help of the size of the frame (see Fig. 4). To measure the stiffness parameters of the tire, the wheel was pulled at its center point in lateral
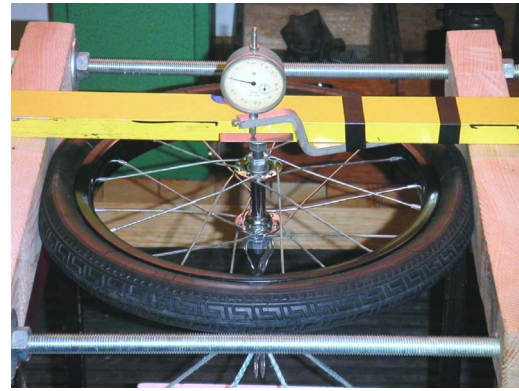

Fig. 4 Stiffness measurement setup

direction with different forces, and the specific lateral stiffness was estimated from the measured displacements of the center point of the wheel relative to the measured contact length in those domains where the characteristics were still linear.

To obtain the damping, the wheel was slightly hit in the lateral direction in the same fixed frame, and the time history of the lateral acceleration of the wheel center point was recorded. The damping factor was identified from the logarithmic decrement of the vibration signal.

The wheel mass moment of inertia with respect to its diameter was determined via time period measurements in simple pendulum experiments.

4.2 Experimental Rig. The identification of the stability chart requires the appropriate tuning of some parameters on the experimental device, namely, the caster length, the contact length, the mass moment of inertia, and the towing speed. Since all of the dimensionless parameters depend on the caster length and the contact length, the proper variation of the system parameters needs special attention.

The experimental rig can be seen in Fig. 5. It shows how the towing speed was varied with the help of a controlled conveyor belt, how the caster length was adjusted, and how the mass moment of inertia of the whole structure was tuned with the help of an additional mass attached at a variable position of the rear part of the caster. The contact length was secured precisely with the help of the tire pressure and the vertical load on the wheel.

In order to avoid the combination of belt and tire oscillations, the conveyor belt was stiffened laterally by a steel frame and the possible lateral buckling of the belt was also under control.
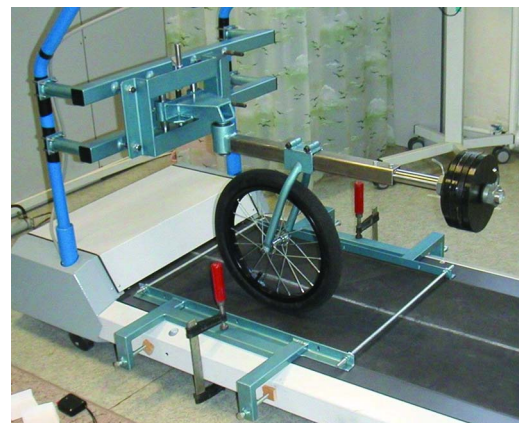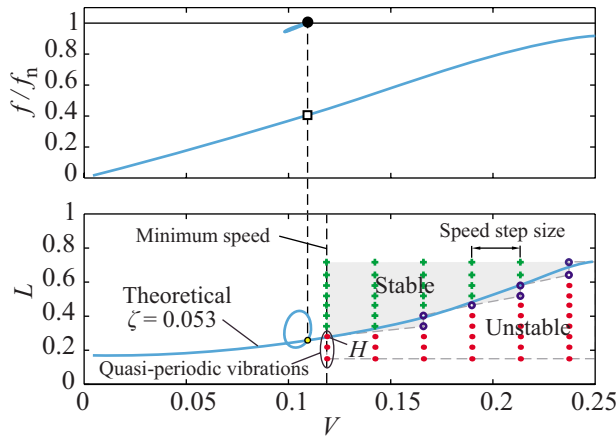

Fig. 5 Experimental rig

Journal of Computational and Nonlinear Dynamics
JULY 2009, Vol. 4 / **031007-3**

Fig. 6 Experimental stability chart

Table 1 The parameters of the system at point _H_

Dimensional parameters
$l=11$ mm
$k=345$ kN/m^2
$J_A=0.0795$ kg m^2
$f_n=2.360$ Hz
$a=39.5$ mm
$b=2.48$ kN s/m^2
$v=0.5$ km/h
Dimensionless parameters
$V=0.118$
$L=0.280$
$\zeta=0.053$

4.3 Measurements. During the experiments, the wheel was towed with different but constant speeds, while the vibrations of the caster and the stability of the system were observed at different but fixed values of the dimensionless parameters. Despite of all our efforts to design the system for a wide range of parameters, we managed to identify only one of the stability boundaries due to the intricate connections of the relatively large number of parameters. Namely, in order to extend the unstable islands in the stability charts, we intended to decrease the damping ratio ζ of our system by increasing the mass moment of inertia with an added mass on the caster, as shown in Fig. 5 (see also Eq. (10)). This way, we also decreased the natural frequency f_n of the system, and the values of the dimensionless towing speeds V were increased (see Eq. (9)). Regarding the minimum speed limit (0.5 km/h) of the conveyor belt, this procedure blocked the experimental investigation in that part of the stability chart where multiple unstable islands exist. Nevertheless, the measured stability boundary was the most relevant one, and we could steer the parameters close enough to one of the double Hopf points.

The experimental results show good agreement with the theoretical ones for low caster lengths. The lower part of Fig. 6 presents the experimentally determined stability limits together with the theoretical prediction that is a small segment of the full stability chart of Fig. 3. In the figure, the dots and crosses refer to linearly unstable and stable systems, respectively. The circles show the experimentally detected stability boundary. At the minimum adjustable towing speed, the double Hopf stability boundary was just approached.

Above the experimental chart of Fig. 6, the theoretical vibration frequencies at the stability boundaries are also presented by continuous lines. Close to the intersection of two theoretical stability boundaries, beating was obs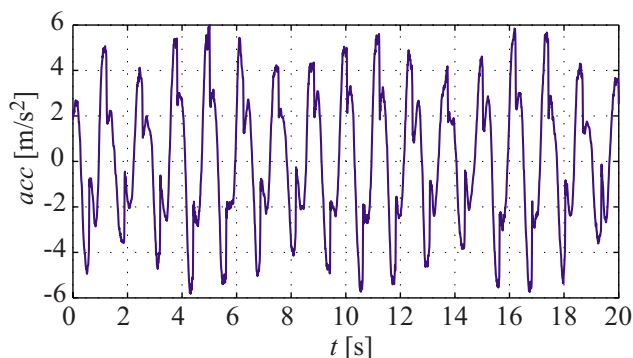erved during the shimmying of the wheel in the encircled parameter domain. These quasiperiodic oscillations could be explained by the theoretical frequency components at the double Hopf point. However, the deeper analysis of the corresponding vibration signals referred to a much more complicated phenomenon.

4.4 Quasiperiodic Signal Analysis. The time history of the acceleration of the end point of the caster was detected by means of a piezo-accelerometer and recorded in the dynamical measurements system PULSE. A typical time history of this signal is shown in Fig. 7, when the parameters are set at the above described critical double Hopf point H in Fig. 6. The parameters of the system are given in Table 1. In Fig. 7, an intricate beating effect can clearly be observed.

The corresponding spectrum produced by the fast Fourier transformation is shown in Fig. 8. There are some distinctive peaks in the spectrum. Two of these at $f_\square=0.969$ Hz and $f_\bullet=2.406$ Hz coincide almost perfectly with the ones determined by the theoretical analysis of the linearized system and which are also shown by the corresponding $\square$ and $\bullet$ symbols in Fig. 6.

In the spectrum of Fig. 8, the largest peak, however, is at $f_\circ=0.802$ Hz, which is just one-third of the larger Hopf frequency $f_\bullet$. The appearance of this lower harmonic together with the two side-peaks around the larger Hopf frequency clearly refers to complex nonlinear vibrations. It was suspected that even the linear quasiperiodic oscillation becomes unstable, and the nonlinear effect of partial sliding in the contact region provide limits for the increasing vibrations resulting in a complicated attractor.
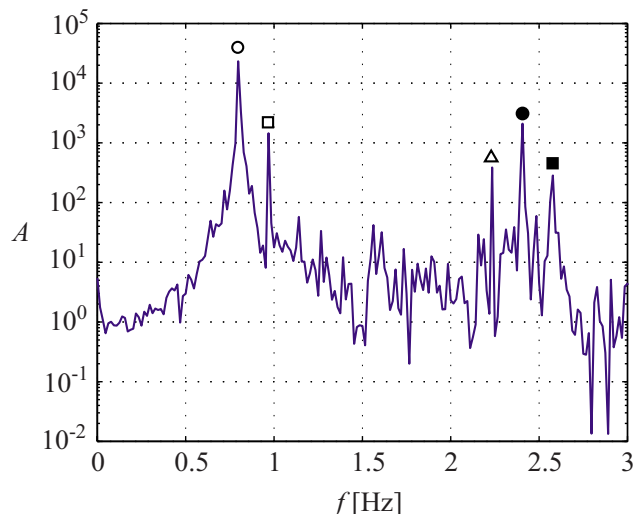

Fig. 7 Acceleration time history for parameter point _H_

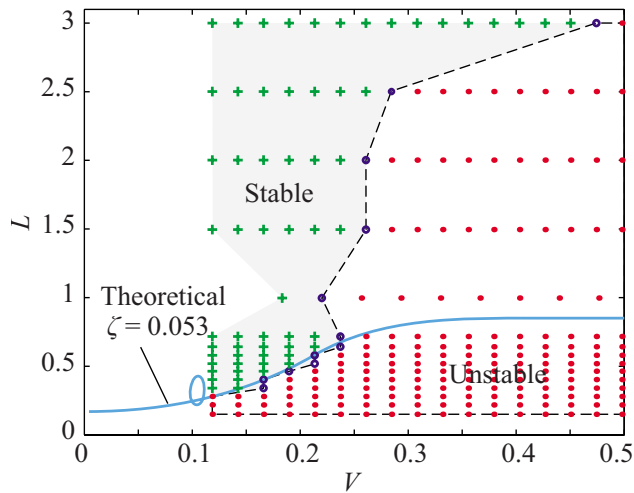Fig. 8 Acceleration spectrum for parameter point _H_

Fig. 9 Global experimental stability chart

5 Discrepancies in the Global Chart

It must be also noted that the experimental stability chart shows substantial difference to the theoretical prediction for higher towing speeds and caster lengths (see Fig. 9). The unexpected unstable behavior at the upper right part of the stability chart could partly be explained by the nonperfect lateral stiffening of the conveyor belt. However, our preliminary investigations indicate that an improved stretched-string tire model using nonzero relaxation length [18] can also explain most of these differences. Nevertheless, this part of the stability chart needs further study from modeling, theoretical analysis, and experimental viewpoints.

6 Partial Sliding as Nonlinearity

For the theoretical explanation of the experienced nonlinear vibrations, a reliable nonlinear mathematical model is needed. Since the experimental results convinced us that the sliding of the contact points has a key role, we decided to use the equations of motion, Eqs. (1) and (4), together with checking the lateral forces in the contact region whether they stay within the condition of sticking, that is, whether they are smaller than the corresponding normal forces multiplied by the static coefficient of friction μ_s. When this condition does not hold, the lateral contact forces decrease to the value of sliding friction forces, that is, to normal

forces multiplied by the dynamic coefficient of friction μ_d. Of course, this kind of model can be solved only numerically.

First, the Runge–Kutta based numerical simulation was applied without the sliding effect ($\mu_s \rightarrow \infty$). Clearly, the linear equations resulted in vibrations increasing exponentially without limits in the unstable parameter domain of the stability chart of Fig. 3. When the geometrical nonlinearities were taken into account in Eq. (4), a stable limit cycle was detected for the same parameters of the chart. However, the deformations of the tire contact region were unrealistically large at the rear end of the contact region. This also confirmed our hypothesis based on the experiments, namely, that the nonlinear effect of partial sliding in the contact region must be the relevant nonlinear effect.

In order to simulate shimmy with partial sliding in the contact region, we use the criterion of Pacejka [18] that was developed during the derivation of the creep-force idea. The normal force distribution in the contact patch is approximated by a parabolic function. Because the stiffness of the tire is linear in our model, the critical deformation is described by

$$|q_{cr}(x)| = \frac{3}{4} \mu_s \frac{F_z}{ak}\left(1 - \frac{x^2}{a^2}\right) \tag{13}$$

where F_z is the overall normal force, and the viscous damping forces are neglected.

7 Simulation Results

Some interesting parts of the stability chart of Fig. 3 were checked by the above described numerical simulation of the nonlinear PDE-IDE system (Eqs. (1) and (4)) extended with condition (Eq. (13)) of partial sliding. The numerical method is essentially a second order Runge–Kutta method in time, while the space discretization with respect to x is tuned to the time steps by implementing the Courant–Friederichs–Lewy stability condition [21] used for the simulation of traveling waves.

Instead of presenting the many intricate nonlinear vibration phenomena that we experienced numerically, only those results are given below, which are related to the experimentally observed quasiperiodic vibration at the parameter point H in the chart of Fig. 6. Thus, the parameters were fixed in the simulation software for the values of the real structure at point H (see Table 1). The initial conditions for the numerical simulations were set in many different ways, but the results shown below correspond to zero initial deformation $q(x,0) \equiv 0$ and caster angle $\psi(0) = 0$, but nonzero $\dot{\psi}(0)$ (rad/s) angular velocity of the caster. This is a good model of an impactlike perturbation of stationary rolling. Since
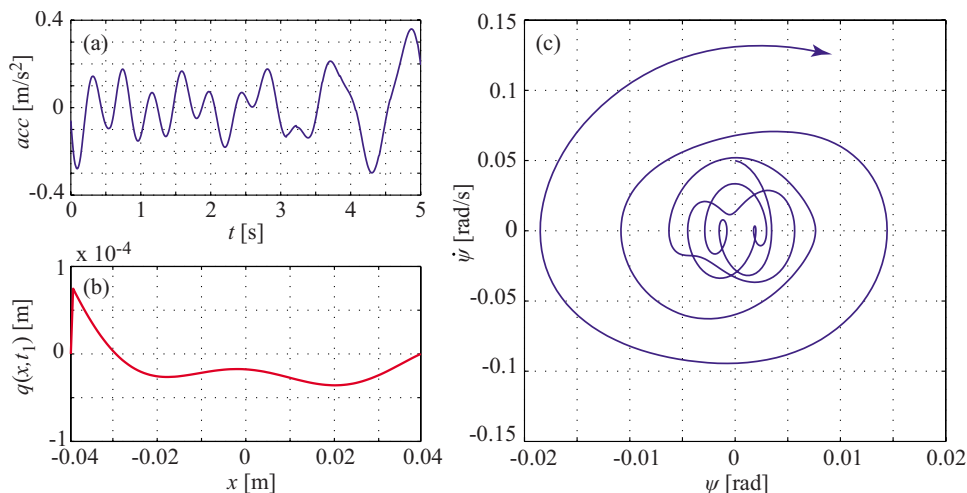

Fig. 10 Simulated transient motion: (a) transient time history of caster end-point acceleration, (b) transient shape of contact line, and (c) 2D projected phase portrait of the transient motion
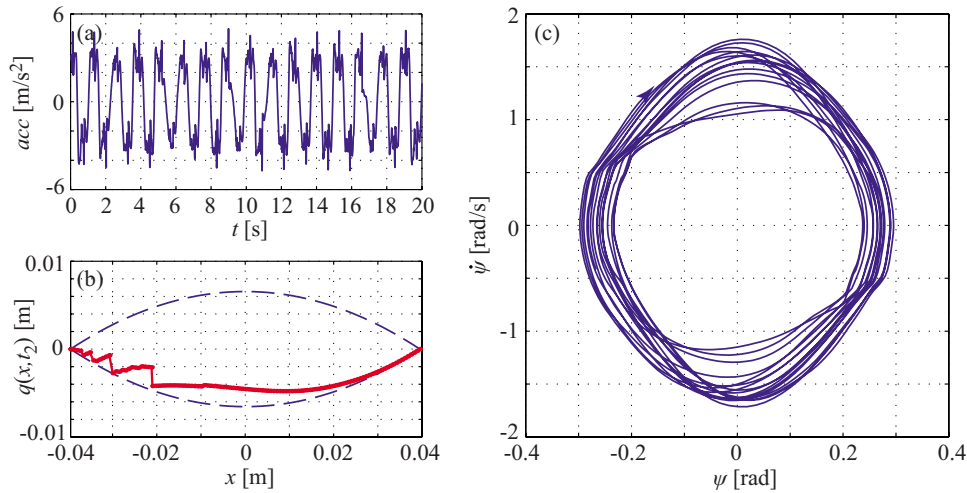
Fig. 11 Simulated stationary motion: (a) stationary time history of caster end-point accelera-tion, (b) shape of the contact line deformed by several slidings, and (c) 2D projected stationary phase portrait

the accelerometer was placed at the end point of the caster during the experiments, the time history of the acceleration of this point is shown in Fig. 10(a). The same transient is presented by the trajectories in Fig. 10(c) in a two-dimensional projection $(\psi, \dot{\psi})$ of the infinite dimensional phase space of the PDE-IDE (or the DDE) system. This transient vibration contains the two theoretical linear vibration frequencies $f_\square$ and $f_\bullet$ at the double Hopf bifurcation point. These are clearly identified in the front spectrum of the waterfall diagram of Fig. 13 right after the first 5 s.

The linearized DDE model (Eq. (8)) has already been simulated and the shapes of the contact line were determined also analyti-cally at different unstable regions of the stability chart [22]. Dur-ing the above transient motion, the simulated shape of the contact line shown in Fig. 10(b) follows almost perfectly the linear pre-dictions apart of a tiny region at the rear part (see the kink at the left side in the figure) where sliding occurs.

According to the simulation results, a kind of stationary motion appears after about 30–40 s. This stationary motion is, however, quite complex in accordance with our experimental observations in Figs. 7 and 8. The simulated stationary time history of Fig. 11(a) is seemingly very similar to that of the experimental one in Fig. 7 both qualitatively and quantitatively. The only difference is

that the simulated signal is somewhat noisier. This is probably caused by the weakness of the brush model, namely, that the tire contact points slide separately leaving kinks behind them in the contact shape (see also Fig. 11(b)).

This chaoticlike motion can also be followed with the help of the corresponding trajectory in the 2D projected phase space of Fig. 11(c).

The spectrum of this stationary vibration at about 50 s is shown in Fig. 12. The similarity between the measured (see Fig. 8) and the simulated (see Fig. 12) spectrum is visible; all the important peaks show up in it as described during the explanation of the experimental spectrum in the subsection on quasiperiodic signal analysis. The corresponding peaks are denoted by the same sym-bols at the very same frequencies. The spectrum in Fig. 12 can also be seen on the waterfall diagram of the signal's wavelet trans-formation in Fig. 13 at about 50 s.

Some of the peaks in the spectrum of Fig. 12 can be explained with the help of Fig. 11(b), which shows a typical contact line shape with many sliding parts in the vicinity of the kinks, and also the sliding limit (blue dashed line) according to formula Eq. (13). The continuous red curves refer to sticking points. The maximum lateral friction forces belong to the maximum lateral deformation (blue dashed line), and they are calculated with the measured static coefficient of friction $\mu_s = 0.7$ while the constant overall ver-tical load is just $F_z = 170$ N. At the kinks, the tire (brush) points
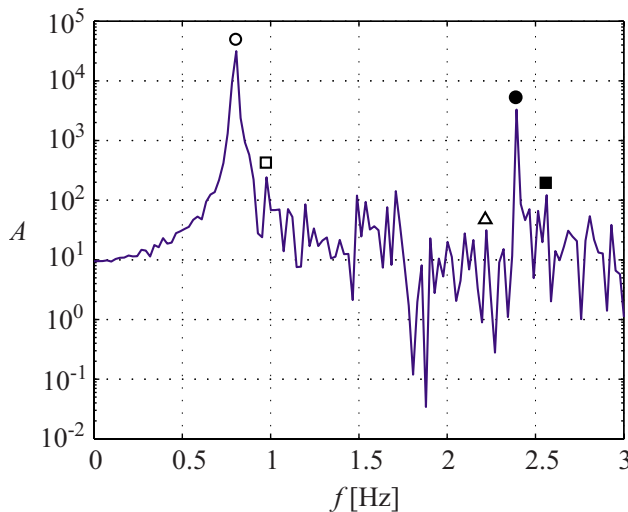

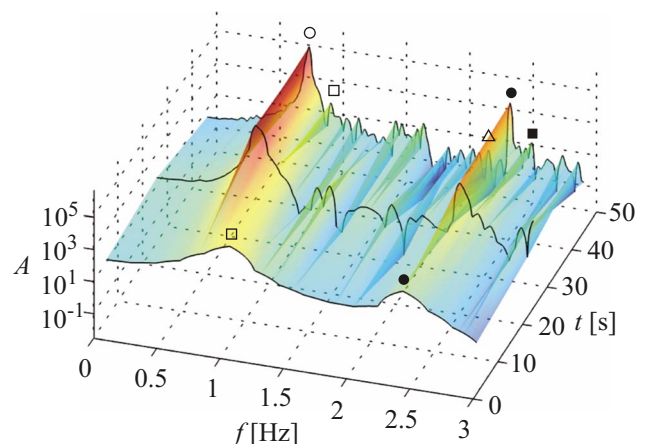**Fig. 12 Spectrum of the simulated stationary quasiperiodic vibration**

Fig. 13 Waterfall diagram of the simulated motion

slide back to a position determined by the dynamic (or sliding) coefficient of friction $\mu_d=0.2$ (its usual value is in the range of 30% of the static coefficient of friction). The peaks $\square$ and $\bullet$ correspond to the linear self-excited frequencies. They show up in this strongly nonlinear vibration of large amplitude because cca 70% of the contact shape survives without sliding in Fig. 11(*b*) and the shape of this front part is quite similar to the shape predicted by the linear theory or by transient simulation in Fig. 10(*b*).

The strongest peak at $f_\bigcirc$ is just at one-third of the larger self-excited vibration frequency $f_\bullet$ in the same way as experienced during measurements. We could not explain this based on our experiments only, but the study of the simulated (and animated) variation of the contact line gives some hint. The front part of the contact line does its snakelike oscillation without sliding for some short periods while its shape is close to the linearly predicted one and its amplitude is increasing. When its amplitude reaches the sliding limit at certain points, this piece goes through a crisis and the appearance of the kinks fragments its shape. This results in the overall frequency $f_\bigcirc$.

It is also interesting to observe that two side-peaks appear during the stationary oscillation at $f_\triangle$ and $f_\blacksquare$ around $f_\bullet$. They might refer to a combination of beating effects originated in some complicated nonlinear coupling, since their distances from the larger self-excited vibration frequency $f_\bullet$ are just the same as the distance of the smaller self-excited vibration frequency $f_\square$ and the third of larger one $f_\bullet$.

The wavelet transformation shows the birth of the peak at $f_\bigcirc$ and the growth of $f_\bullet$ and its side-peaks. The lower self-excited vibration frequency $f_\square$ diminishes then grows again due to the fragmentation effect explained above. It disappears and shows up again and again every 20–30 s quite randomly.

8 Conclusion

The experimental results, the linear stability theory, and the simulation results of the extended nonlinear PDE-IDE (or DDE) model show very good agreement at one of the most intricate parameter points of the wheel shimmy, where the linear theory predicts quasiperiodic self-excited oscillations originated in a double Hopf bifurcation. After the transients, however, the increasing nonlinear vibrations are somewhat stabilized at another more complex quasiperiodic motion, which contains at least five characteristic peaks in its spectrum. These are identified both by experiments and by simulations, the latter giving some hints about their possible physical origin. The clarification of this picture could be supported by a full analytical unfolding of the co-dimension two Hopf bifurcation.

These results confirm the relevance of the memory effect in tire models during the investigation of stability problems of wheels.

References

[1] Pritchard, J., 2001, "Overview of Landing Gear Dynamics," J. Aircr., **38**(1), pp. 130–137.
[2] Broulhiet, G., 1925, "The Suspension of the Automobile Steering Mechanism: Shimmy and Tramp," Bull Soc. Ing. Civ. Fr., **78**, pp. 540–554.
[3] de Lavaud, D. S., 1927, "Shimmy, Pseudo-Shimmy and Tramp of an Automobile," Acad. Sci., Paris, C. R., **185**, pp. 254–257.
[4] Sura, N. K., and Suryanarayan, S., 2007, "Closed-Form Analytical Solution for the Shimmy Instability of Nose-Wheel Landing Gears," J. Aircr., **44**(6), pp. 1985–1990.
[5] Coetzee, E., 2006, "Shimmy in Aircraft Landing Gear," Tech. Report No. 56/2006, http://www.smithinst.ac.uk/Projects/ESGI56/ESGI56-AirbusShimmy/Report.
[6] Thota, P., Krauskopf, B., and Lowenberg, M., 2008, "Shimmy in a Nonlinear Model of an Aircraft Nose Landing Gear With Non-Zero Rake Angle," Proceedings of ENOC-2008, Russia.
[7] Sharp, R. S., Evangelou, S., and Limebeer, D. J. N., 2004, "Advances in the Modelling of Motorcycle Dynamics," Multibody Syst. Dyn., **12**(3), pp. 251–283.
[8] Catani, G., and Mancinelli, N., 2007, "Motorcycle Local Stability Analysis Under Acceleration and Braking by Model Linearization and Eigenproblem Solution," Proceedings of IDECT/CIE-2007, ASME, Las Vegas, NV.
[9] Troger, H., and Zeman, K., 1984, "A Nonlinear-Analysis of the Generic Types of Loss of Stability of the Steady-State Motion of a Tractor-Semitrailer," Veh. Syst. Dyn., **13**(4), pp. 161–172.
[10] Sharp, R. S., and Fernańdez, M. A. A., 2002, "Car-Caravan Snaking—Part 1: The Influence of Pintle Pin Friction," Proc. Inst. Mech. Eng., Part C: J. Mech. Eng. Sci., **216**(7), pp. 707–722.
[11] Schlippe, B., and Dietrich, R., 1941, "Das Flattern eines bepneuten Rades (Shimmying of a Pneumatic Wheel)," *Bericht 140 der Lilienthal-Gesellschaft für Luftfahrtforschung*, pp. 35–45, 63–66. (English translation is available in NACA Technical Memorandum 1365, pp. 125–166, 217–228, 1954).
[12] Sharp, R. S., and Jones, S. J., 1980, "A Comparison of Tyre Representations in a Simple Wheel Shimmy Problem," Veh. Syst. Dyn., **9**(1), pp. 45–47.
[13] Limebeer, D. J. N., Evangelou, S., and Sharp, R. S., 2001, "Stability of Motorcycles Under Acceleration and Braking," Proceedings of DETC'01, ASME, Pittsburgh, PA, pp. 1–3.
[14] Stepan, G., 1998, "Delay, Nonlinear Oscillations and Shimmying Wheels," *Proceedings of Symposium CHAOS'97*, Kluwer, Ithaca, NY, pp. 373–386.
[15] Esmailzadeh, E., and Farzaneh, K. A., 1999, "Shimmy Vibration Analysis of Aircraft Landing Gears," J. Vib. Control, **5**, pp. 45–46.
[16] Stepan, G., 1991, "Chaotic Motion of Wheels," Veh. Syst. Dyn., **20**, pp. 341–351.
[17] Takacs, D., Stepan, G., and Hogan, S. J., 2008, "Isolated Large Amplitude Periodic Motions of Towed Rigid Wheels," Nonlinear Dyn., **52**(1–2), pp. 27–34.
[18] Pacejka, H. B., 2002, *Tyre and Vehicle Dynamics*, Elsevier, Burlington MA.
[19] Pacejka, H. B., and Bakker, E., 1991, "The Magic Formula Tyre Model," Veh. Syst. Dyn., **21**, pp. 1–18.
[20] Stepan, G., 1989, *Retarded Dynamical Systems*, Longman, Essex, England.
[21] Lax, P. D., and Wendroff, B., 1960, "Systems of Conservation Laws," Commun. Pure Appl. Math., **13**(2), pp. 217–237.
[22] Takacs, D., and Stepan, G., 2006, "Dynamic Contact Problem of Rolling Elastic Wheels," Proceedings of ICGF 2006.